MNRAS 000, 1–15 (2022) Preprint 30 December 2022 Compiled using MNRAS LaTeX style file v3.0

local primordial non-Gaussianity from the large-scale clustering of photometric DESI luminous red galaxies

Mehdi Rezaie[1,2], Ashley J. Ross[3], Hee-Jong Seo[2], Hui Kong[3], Edmond Chaussidon[4], Anna Porredon[3], Lado Samushia[1], Rongpu Zhou[5], Alex Krolewski[6,7,8], Arnaud de Mattia[4], Jose Bermejo[?], Florian Beutler[9], Christophe Yeche[4], Nathalie Palanque-Delabrouille[4,5], Klaus Honscheid[3,10], and DESI Builders

[1]*Department of Physics, Kansas State University, 116 Cardwell Hall, Manhattan, KS 66506, USA*
[2]*Department of Physics and Astronomy, Ohio University, Athens, OH 45701, USA*
[3]*Center for Cosmology and AstroParticle Physics, The Ohio State University, 191 West Woodruff Avenue, Columbus, OH 43210, USA*
[4]*IRFU, CEA, Universite Paris-Saclay, F-91191 Gif-sur-Yvette, France*
[5]*Lawrence Berkeley National Laboratory, 1 Cyclotron Road, Berkeley, CA 94720, USA*
[6]*Department of Physics and Astronomy, University of Waterloo, 200 University Ave W, Waterloo, ON N2L 3G1, Canada*
[7]*Perimeter Institute for Theoretical Physics, 31 Caroline St. North, Waterloo, ON N2L 2Y5, Canada*
[8]*Waterloo Centre for Astrophysics, University of Waterloo, 200 University Ave W, Waterloo, ON N2L 3G1, Canada*
[9]*Institute for Astronomy, University of Edinburgh, Royal Observatory, Blackford Hill, Edinburgh EH9 3HJ, UK*
[10]*Department of Physics, The Ohio State University, 191 West Woodruff Avenue, Columbus, OH 43210, USA*

Accepted XXX. Received YYY; in original form ZZZ

ABSTRACT

This paper uses the large-scale clustering of luminous red galaxies selected from the Dark Energy Spectroscopic Instrument Legacy Imaging Surveys Data Release 9 to constrain the local primordial non-Gaussianity (PNG) parameter $f_{\rm NL}$. Using the angular power spectrum, we thoroughly investigate the impact of various photometric systematic effects, such as those caused by Galactic extinction and varying survey depth. Simulations are utilized to construct covariance matrices, evaluate the robustness of our pipeline, and perform statistical tests to assess whether spurious fluctuations are properly mitigated and calibrated. Using modes from $\ell = 2$ to 300, we find $X1 < f_{\rm NL} < X2$ with our conservative and $X1 < f_{\rm NL} < X2$ with extreme treatment of imaging systematics, both at 68% confidence. While our results are consistent with zero PNG, but we show that the understanding of imaging systematics is of paramount importance to obtain unbiased constraints on $f_{\rm NL}$.

Key words: cosmology: inflation - large-scale structure of the Universe

1 INTRODUCTION

Current observations of the cosmic microwave background (CMB), large-scale structure (LSS), and supernovae (SN) are explained by a cosmological model that consists of dark energy, dark matter, and ordinary luminous matter, which has gone through a phase of rapid expansion, known as *inflation*, at its early stages (see, e.g., Weinberg et al. 2013). The theory of inflation elegantly addresses fundamental issues with the hot Big Bang theory, such as the isotropy of the CMB temperature, absence of magnetic monopole, and flatness of the Universe (see, e.g., Ryden 2002). At the end of inflation, the Universe was reheated and primordial fluctuations are generated to seed the subsequent growth of structure (Kofman et al 1994, Bassett et al 2006, Lyth and Liddle 2009). While the presence of an inflationary era is certain but the details of the inflation field still remain highly unknown, and statistical properties of primordial fluctuations pose as one of the puzzling questions in modern observational cosmology. Analyses of cosmological data have revealed that initial conditions of the Universe are consistent with Gaussian fluctuations (Guth and Kaiser 2005); however, there are some classes of models that predict some levels of non-Gaussianities in the primordial gravitational field. In its simplest form, primordial non-Gaussianity depends on the local value of the gravitational potential ϕ and is parameterized by a nonlinear parameter $f_{\rm NL}$ (Komatsu & Spergel 2001),

$$\Phi = \phi + f_{\rm NL}[\phi^2 - <\phi^2>]. \tag{1}$$

Standard slow roll inflation predicts $f_{\rm NL}$ to be of order 10^{-2}, while multifield theories predict considerably higher values than unity (see, e.g., Putter et al 2017). Therefore, a robust measurement of

$f_{\rm NL}$ can be considered as the first stepping stone toward better understanding the physics of the early Universe. PNG alters local number density of galaxies by coupling the long and small wavelength modes of dark matter gravitational field, and as a result it introduces a scale-dependent shift in halo bias (see, e.g., Dalal et al. 2008; Slosar et al. 2008),

$$\Delta b \sim f_{\rm NL}\frac{(b-p)}{k^2}, \tag{2}$$

where p determines the response of the tracer to the halo gravitational field. Assuming universality of the halo function, i.e., the occupation of halos can be determined from the mass, $p = 1$. However, numerical simulations have shown the halo mass function of tracers that are result of recent mergers could depend on more parameters other than mass, and thus $p = 1.6$. Because of the k^{-2} dependence, the effect of local primordial non-Gaussianity leaves its signature on the large scales in the two-point clustering of large-scale structure.

Current tightest bound on $f_{\rm NL}$ comes from the three-point clustering analysis of the CMB temperature anisotropies by the Planck satellite, $f_{\rm NL} = 0.9 \pm 5.0$ (Akrami et al. 2019). Next generations of CMB experiments, will improve this constraint but since CMB is limited by cosmic variance, it alone cannot further enhance to break the degeneracy amongst inflationary models (see, e.g., Ade et al 2019). However, combining CMB with LSS data could cancel cosmic variance, partially if not completely, and enhance these limits to a precision level required to differentiate between various inflationary models (see, e.g., Schmittfull & Seljak 2018). Constraining $f_{\rm NL}$ with the three point clustering of LSS is also hindered by the late-time nonlinear effects raised due to structure growth (see, e.g., Baldauf et al 2011), and this leaves the scale-dependent bias effect a smoking gun for constraining local PNG with LSS.

Measuring $f_{\rm NL}$ using the scale-dependent bias is however very challenging due to the presence of systematic effects which cause excess clustering signal on the same scales sensitive to $f_{\rm NL}$. These systematics can be broadly classified into theoretical and observational. Major theoretical systematic effects are caused by the geometry of survey – a fact that we never observe the full night sky – which results in coupling different angular modes (see, e.g., Beutler et al. 2014, de Mattia and Ruhlmann-Kleider 2019). The other effect is commonly referred to as integral constraint and is raised due to our estimation of the mean density directly from data itself, which pushes the clustering signal on modes near the size of survey to zero (Peacock and Nicholson 1991, Wilson et al 2015). Ignoring any of these effects leads to biased $f_{\rm NL}$ constraints (see, e.g., Riquelme et al 2022). On the other hand, observational systematics are primarily caused by varying imaging properties across the sky or calibration issues which leave spurious fluctuations in target density field (see, e.g., Huterer et al 2013). This type of systematic error is much more difficult to handle and has hindered previous studies of local PNG with galaxy and quasar clustering (see, e.g., Ho et al. 2015). For instance, Pullen & Hirata (2013) found that the level of systematic contamination in the quasar sample of SDSS DRX does not allow a robust $f_{\rm NL}$ measurement. These imaging systematic issues are expected to be severe for wide-area galaxy surveys that observe the night sky closer to the Galactic plane and attempt to loosen the selection criteria to incorporate fainter targets. Beside canceling cosmic variance, cross correlating different tracers is a technique to alleviate systematic error, as each tracer might respond differently to a source of systematics. Giannantonio et al 2014 presents constraints using the integrated Sachs Wolfe effect. McCarthy et al (2022) uses cosmic infrared background as a proxy for halos and cosmic microwave background lensing as a proxy for matter, finding no evidence for local primordial non-Gaussianity.

DESI utilizes robots to collect 5000 spectra simultanously, and it is going to deliver an unparalleled amount of spectroscopic data up to redshift X, which will complete our understanding of the energy contents of the Universe. With the volume probed and assuming imaging systematics are under control, DESI along with other upcoming surveys such as Rubin Observatory, and SphereX are forecast to yield unprecedented constraints on $f_{\rm NL}$ as well (Abell et al 2009, Dore et al 2014, Aghamousa et al 2016). DESI preselects its targets from its dedicated imaging surveys, as known as Legacy Surveys, which are collected between 2014 and 2019 from three ground-based telescopes in Chile and the US. Understanding and calibration of systematic error in DESI imaging data is of paramount importance since these effects from imaging catalogs could potentially be inherited into spectroscopic catalogs, and thus impact the science one can do with DESI data. DESI targets galaxies and quasars and the effect of observational systematics in the DESI imaging data have been studied in great detail in Kitanidis et al (???), Rezaie et al (2021), Zhou et al (2021), and Chaussidon et al (2022). Improving methods to characterize systematic error in these samples is also important for measuring $f_{\rm NL}$. We have a lot of amazing methods to eliminate the effect of imaging systematics. Some of these methods are based on cross correlating the map of target density with maps for imaging properties, while the other methods use a regression analysis to regress out the modes of imaging properties from the target density. While these methods are essentially the same, but they have their own limitations and constraints. For instance the cross correlation techniques can only be used for 2D data and could be time consuming for a large survey, but the template-based regression methods could be fast but yield biased results or remove some of the true clustering signal. Specifically related to the regression based methods, there is a little effort to calibrate and characterize the amount of the true clustering signal which is removed during the cleaning process. For studies like BAO and RSD, these effect might not matter (see, e.g., Merz et al 2021), however, as these effects are very prominent on large scales (see, e.g., Rezaie et al 2020, Mueller et al 2022), they could introduce biases in $f_{\rm NL}$ constraints.

With the high importance of systematic error, the primary focus of this paper is to present an exquisite study of imaging systematic error and characterization of mitigation biases for measuring $f_{\rm NL}$. We also present enhanced statistical tools to address the data quality and significance of residual systematic error. In this paper, we use the photometric sample of luminous red galaxies from the DESI Legacy Imaging Surveys Data Release 9, hereafter referred to as DR9, to constrain the local primordial non-Gaussianity parameter $f_{\rm NL}$, while testing the robustness of our results against various sources of systematic effects. We also make use of spectroscopic data from DESI Survey Validation to determine the redshift distribution of galaxies. We cross correlate the DR9 density field with the templates of imaging realities to assess the effectiveness of treatment methods and to characterize the significance of residual systematic error. Section 2 describes the DR9 sample and simulations with and without PNG and imaging systematic effects, and Section 3 outlines the theory for modeling angular power spectrum and analysis techniques for quantifying various observational systematic effects. Finally, we present the results in Section 4, and conclude with a comparison to previous $f_{\rm NL}$ constraints in Section 5.

2 DATA

Luminous red galaxies (LRGs) are massive galaxies that occupy massive halos, lack active star formation, and are considered as one of the highly biased tracers of large scale structure. Redshift of LRGs can be easily determined from a break around 4000 Å in their spectra. LRGs are widely targeted in previous galaxy redshift surveys (see, e.g., Eisenstein et al 2001, Prakash et al 2016), and their clustering and redshift properties are well studied (see, e.g., Reid et al 2016). DESI is expected to collect spectra of millions of LRGs covering the redshift range of $0.4 < z < 1.0$ over the span of its five year mission. Targets for DESI spectroscopy are selected from imaging surveys; The ground-based surveys that probe the sky in the optical bands are the Mayall z-band Legacy Survey using the Mayall telescope at Kitt Peak (see e.g. Dey et al. 2018), the Beijing–Arizona Sky Survey using the Bok telescope at Kitt Peak (Zou et al. 2017), and the DECam Legacy Survey (DECaLS;Flaugher et al. 2015) on the Blanco 4m telescope. Additionally, the Legacy Surveys program incorporates observations conducted from the same instrument under the Dark Energy Survey (Dark Energy Survey Collaboration; Fermilab & Flaugher 2005), which constitutes for about 1130 deg^2 of their southern sky footprint. The BASS+MzLS footprint can be distinguished from the DECaLS by applying DEC > 32.375 degrees, although there is an overlap between the two region for calibration.

2.1 DR9 LRGs

We use photometric LRGs selected from the DESI Imaging Surveys Data Release 9 (DR9; Dey et al. 2018) using the selection designed for the DESI 1% survey (Dawson et al 2022), described as SV3 in Zhou et al. (2022). The color-magnitude cuts are described in the g, r, z bands in the optical and $W1$ band in the infrared, and summarized here in Tab. 1. The implementation of these selections in the DESI pipeline is described in Myers et al (2022). DESI-like LRGs are selected brighter than the survey depth limits, and thus the sample density field is nearly homogenous. To further reduce stellar contamination, the sample is masked for bright stars, foreground bright galaxies as well as clusters of galaxies [1]. Then, it is binned into HEALPIX (Gorski et al. 2005) at NSIDE = 256 to construct the density map with an average density of 800 deg^{-2} with a coverage around 14, 000 square degrees of the sky. The density map is corrected for pixel incompleteness in the density field of LRGS using a catalog of random points, hereafter referred to as randoms, uniformly scattered over the footprint with the same cuts and masks applied to the DR9 LRGs.

Fig. 1 (top) shows observed density field of DR9 LRGs in deg^{-2} before accounting for any potential systematic effects. There are some disconnected islands, hereafter referred to as *spurious islands*, in the DECaLS North region at Declination below −11, which are removed from the sample to minimize potential calibration issues. Additionally, parts of the DECaLS South with Declination below −30 are cut from the sample, since similar calibration issues might tamper with our analysis. We present how these data cuts influence our $f_{\rm NL}$ constraints in Section 4. Fig. 1 (bottom) illustrates the redshift distribution of our sample which is inferred from the DESI Survey Validation data (Dawson et al 2022), and the evolution of galaxy bias for our LRG sample adapted from Zhou et al. (2021), consistent with the assumption of a constant clustering amplitude.

[1] See the maskbits at `https://www.legacysurvey.org/dr9/bitmasks/`

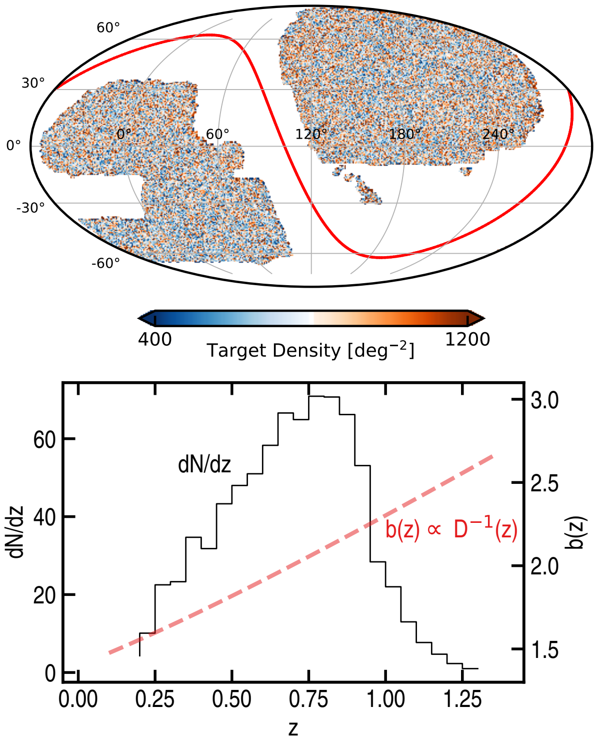

Figure 1. Top: Observed density field of DESI Luminous Red Galaxies Data Release 9 (Dey et al 2018) in deg^{-2} . Spurious disconnected islands from the DECaLS North footprint at Declination below −11 and parts of the DECaLS South with Declination below −30 are dropped from the DR9 sample due to potential calibration issues. Bottom: Redshift distribution and bias evolution of DESI LRGs (Zhou et al. 2021, 2022) (Zhou et al 2021, Zhou et al 2022, Dawson et al 2022). The redshift distribution is deducted from spectroscopy and the bias model assumes a constant clustering amplitude.

We study the impact of potential sources of systematic error, mapped into HEALPIX at the same NSIDE. Similar to Zhou et al. (2022), the properties studied in this work are local stellar density constructed from point-like sources with a g-band magnitude in the range $12 \leq g < 17$ from Gaia Data Release 2 (see, Gaia Collaboration et al. 2018; Myers et al. 2022); Galactic extinction E[B-V] from Schlegel et al. (1998); and other imaging properties include survey depth (galaxy depth in the g, r, and z bands and PSF depth in W1) and seeing in the g, r, and z bands. These maps are produced by making the histograms of randoms (painted with imaging properties) in HEALPix and averaging over randoms in each pixel. Fig. 3 shows the Pearson correlation between galaxy density and imaging properties for the imaging surveys in the top panel and the correlation among imaging properties themselves for the full DESI survey in the bottom panel. There is a strong correlation between galaxy density and depth maps and then the second important property seems to be Galactic foregrounds. There is a little correlation between galaxy density and the W1 depth and psfsize properties. We find that there is a large correlation among the imaging properties themselves, especially between the local stellar density and Milky Way extinction; also, the r-band and g-band properties are more correlated with each other than with the z-band. We follow a template based method to derive a set of weights to account for spurious fluctuations by regressing out galaxy counts against a set of imaging maps or templates. Both linear and nonlinear models are considered to investigate nonlinear systematic error. Parameters of

Table 1. Selection criteria for the DESI-like LRG targets from Zhou et al (2022).

Footprint	Criterion	Description
DECaLS	$z_{\rm fiber} < 21.7$	Faint limit
	$z - W1 > 0.8 \times (r - z) - 0.6$	Stellar rejection
	$[(g - r > 1.3)$ AND $((g - r) > -1.55 * (r - W1) + 3.13)]$ OR $(r - W1 > 1.8)$	Remove low-z galaxies
	$[(r - W1 > (W1 - 17.26) * 1.8)$ AND $(r - W1 > W1 - 16.36)]$ OR $(r - W1 > 3.29)$	Luminosity cut
BASS+MzLS	$z_{\rm fiber} < 21.71$	Faint limit
	$z - W1 > 0.8 \times (r - z) - 0.6$	Stellar rejection
	$[(g - r > 1.34)$ AND $((g - r) > -1.55 * (r - W1) + 3.23)]$ OR $(r - W1 > 1.8)$	Remove low-z galaxies
	$[(r - W1 > (W1 - 17.24) * 1.83)$ AND $(r - W1 > W1 - 16.33)]$ OR $(r - W1 > 3.39)$	Luminosity cut

the models are fit by optimizing the negative Poisson log likelihood, $= \sum \lambda - \rho \log(\lambda)$, where the summation runs over pixels, ρ is the galaxy density, and λ is either a linear or nonliner model for galaxy density given imaging properties $\mathbf{x}$ as input, $\lambda(\mathbf{x}) = \log(1 + e^{f(\mathbf{x})})$. For finding the parameters of the linear model, we perform a Monte Carlo Markov Chain (MCMC) search using the EMCEE package CITE and for the nonlinear model we use the implementation from Rezaie et al (2021); specifically, the nonlinear model is an ensemble of 20 neural network models. Each neural network is constructed with three hidden layers and 20 rectifier units on each layer. Rectifier is identity function for positive input and zero for negative, and it introduces nonlinearities in the neural network. For the linear model we use all data for computing the log of posterior during MCMC while for the nonlinear approach we use 60% of data for training, 20% for validation, and 20% for testing; this is to minimize the chance of over-fitting by the nonlinear model. By changing the permutation of training-testing splits, we test the nonlinear model on entire data. The training is performed for up to 70 training epochs using ADAM optimizer, which is a variant of gradient descent, and the learning rate is tuned on the validation set to dynamically varying between 0.001 and 0.1, to enable learning robust against local minima. The best model is then selected with the lowest prediction error when applied to the validation set. Finally, we apply the ensemble of 20 best fit models to the test set and average over the predictions.

Fig. 2 shows the predicted density fields from the linear model using various sets of imaging maps, and the nonlinear prediction is also shown for comparison. While most of the large-scale spurious fluctuations are explained by just the extinction map and depth in the z band, adding the psfsize in the r band seems to add more fine structure to the predicted density map. Using all maps does not add much structure. Comparing linear to nonlinear with the same input maps, we find that the nonlinear approach yields finer structure due to a higher flexibility. Overall, both models predict higher density near the boundaries where the surveys meet the high extinction regions of Milky Way. These regions are probably contaminated artifacts entering the selection either via the direct stellar contamination or the impact of extinction on colors.

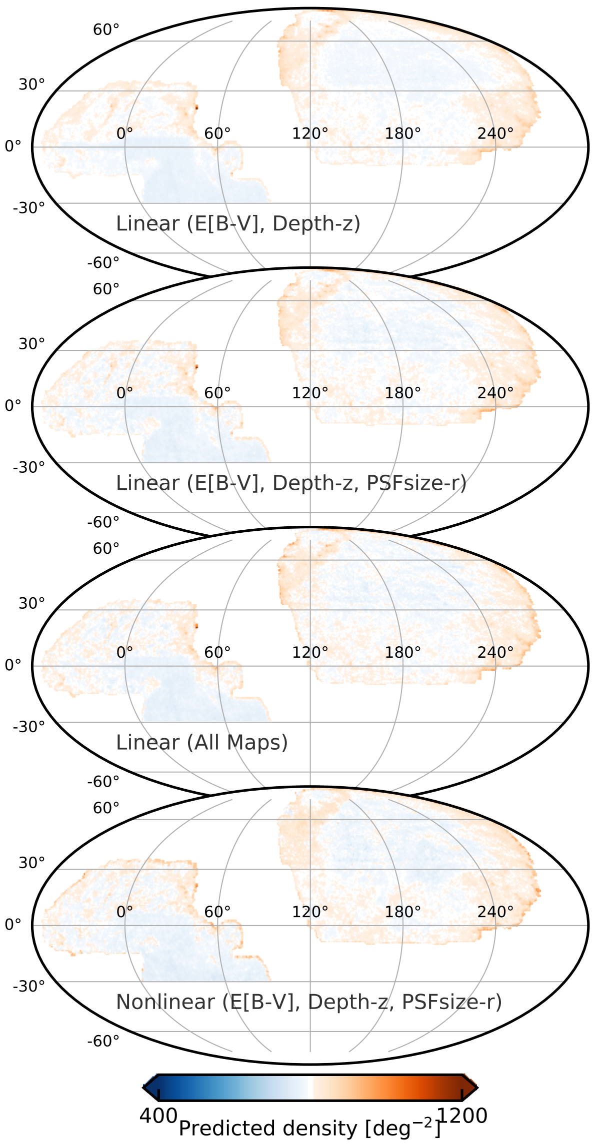

Figure 2. Predicted galaxy counts from template regression. Baseline approach uses imaging maps from Zhou et al. (2022): EBV, galaxy depth in rgz, psfdepth in W1, and psfsize in grz. Conservative I uses EBV and galaxy depth in z, and Conservative II uses EBV, galaxy depth in z, and psfsize in r. In all approaches, the models are regressed on BASS+MzLS, DECaLS North, and DECaLS South separately.

2.2 Lognormal Simulations

Lognormal distributions are shown to be appropriate for describing matter density fluctuations on large scales (Coles & Jones 1991). Unlike N-body simulations, the generation of lognormal density fields is rather quick and enables a computationaly cheap method to create a large number of realizations, validate analysis pipelines, and construct covariance matrices for error estimation. FLASK (Full-sky Lognormal Astro-fields Simulation Kit; Xavier et al. 2016) is used to generate series of lognormal galaxy density fields with $f_{\rm NL} = 0$ and 76.92 using $b(z) = 1.43/D(z)$. 1000 realizations

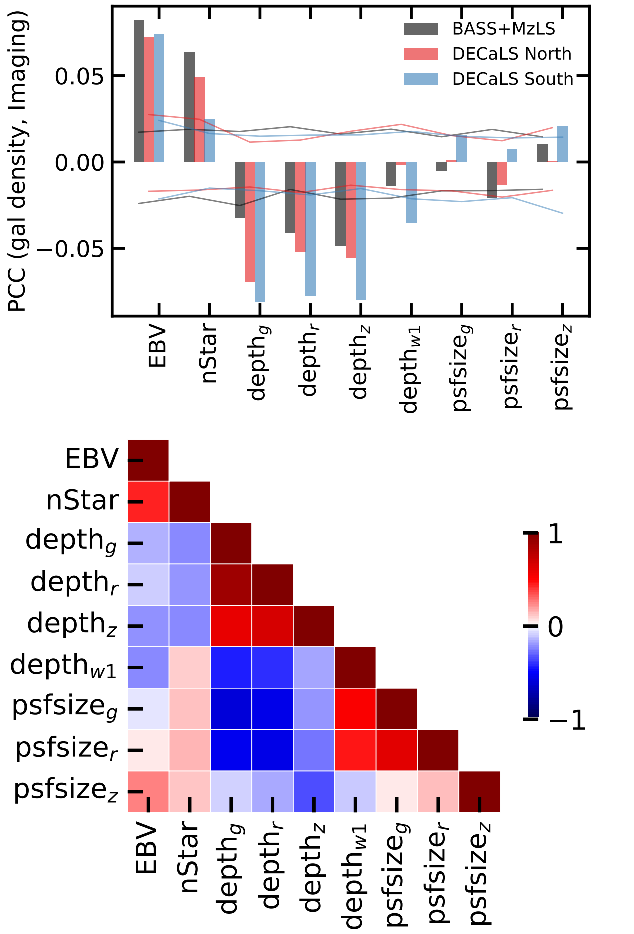

Figure 3. Top: Pearson-r correlation coefficient between galaxy density and imaging properties in the three imaging regions (top) and between imaging properties themselves for the full DESI footprint (bottom). Solid curves represent the range of correlations observed in 100 randomly selected mock realizations.

are generated for each $f_{\rm NL}$. The fiducial cosmology to generate the mocks is based on a flat ΛCDM universe including one massive neutrino with $m_\nu = 0.06$ eV, and the rest of cosmological parameters are chosen within 68% of the Planck 2018 results (Planck 2018),

$h = 0.67, \Omega_M = 0.31, \sigma_8 = 0.8$, and $n_s = 0.97$.

We use the same fiducial cosmology for the analysis of DR9 sample. These parameters are not degenerate with $f_{\rm NL}$, however the impact of the fiducial cosmology on $f_{\rm NL}$ constraints is further investigated in Appendix ?.

3 METHODOLOGY

This section describes the estimator for measuring the angular power spectrum and the methodology for modeling it in the presence of PNG. We also demonstrate how we correct for the effects of survey geometry and integral constraint in the modeling. The statistical tools for measuring the remaining systematic error are also presented.

3.1 Modeling Power Spectrum

The projected angular power spectrum of galaxies in the presence of redshift space distortions and local primordial non-Gaussianity is related to the 3D linear power spectrum $P(k)$ and shotnoise $N_{\rm shot}$ by (see, e.g., Slosar et al. 2008),

$$C_\ell = \frac{2}{\pi}\int_0^\infty \frac{dk}{k} k^3 P(k)|\Delta_\ell(k)|^2 + N_{\rm shot}, \tag{3}$$

where $N_{\rm shot}$ is the scale-independent shotnoise, and $\Delta_\ell(k) = \Delta_\ell^{\rm g}(k) + \Delta_\ell^{\rm RSD}(k)$ with,

$$\Delta_\ell^{\rm g}(k) = \int \frac{dr}{r} r b(r) D(r) \frac{dN}{dr} j_\ell(kr), \tag{4}$$

$$\Delta_\ell^{\rm RSD}(k) = -\int \frac{dr}{r} r f(r) D(r) \frac{dN}{dr} j_\ell''(kr), \tag{5}$$

where $D(r)$ is the normalized growth factor such that $D(0) = 1$, $f(r)$ is the growth rate, r is the comoving distance, dN/dr is the normalized redshift distribution of galaxies[2], $b(r)$ is the linear bias plus the scale-dependent shift due to PNG,

$$b(r) = b + 2(b-p) f_{\rm NL} \alpha \delta_c \tag{6}$$

$\delta_c = 1.686$ is the critical density above which gravitational collapse occurs (Fillmore & Goldreich 1984), . The parameter p is the response of the tracer to halo's gravitational field, e.g., 1 for luminous red galaxies and 1.6 for recent mergers. In order to overcome rapid oscillations in spherical Bessel functions, we employ the FFTLog[3] algorithm and its extension as implemented in Fang et al (2020) to compute the inner integrations over $d\ln r$.

For a galaxy survey that observes the sky partially, the measured power spectrum is convolved with the survey geometry. This means that the pseudo-power spectrum $\hat{C}_\ell$ obtained by the direct Spherical Harmonic Transforms of a partial sky map, differs from the full-sky angular spectrum C_ℓ. However, their ensemble average is related by (**?**)

$$< \hat{C}_\ell >= \sum_{\ell'} M_{\ell\ell'} < C_{\ell'} >, \tag{7}$$

where $M_{\ell\ell'}$ represents the mode-mode coupling from the partial sky coverage. This is known as the Window Function effect and a proper assessment of this effect is crucial for a robust measurement of the large-scale clustering of galaxies. This window effect is a source of observational systematic error and impacts the measured galaxy clustering, especially on scales comparable to survey size.

We follow a similar approach to that of (**?**) to model the window function effect on the theoretical power spectrum C_ℓ rather than correcting the measured pseudo-power spectrum from data. First, we use HEALPIX to compute the pseudo-power spectrum of the window $\hat{C}_\ell^{\rm window}$, which is defined by a mask file in ring ordering format with NSIDE= 256. Then, we transform it to correlation function by,

$$\omega^{\rm window}(\theta) = \frac{1}{4\pi}\sum_\ell (2\ell+1)\hat{C}_\ell^{\rm window} P_\ell(\cos\theta). \tag{8}$$

Next, we normalize $\omega^{\rm window}$ such that it is normalized to one at $\theta =$

[2] $dN/dr = (dN/dz) * (dz/dr) \propto (dN/dz) * H(z)$
[3] github.com/xfangcosmo/FFTLog-and-beyond

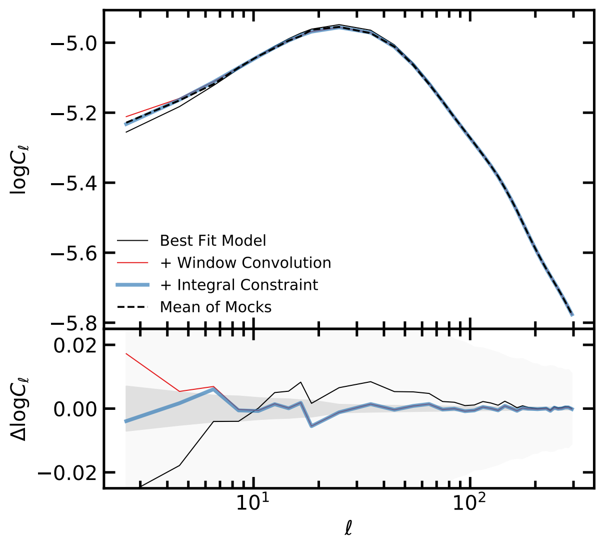

Figure 4. Mean power spectrum of 1000 mocks with $f_{\rm NL}$ = 0 and best fit theoretical prediction after accounting for various theoretical systematic effects.

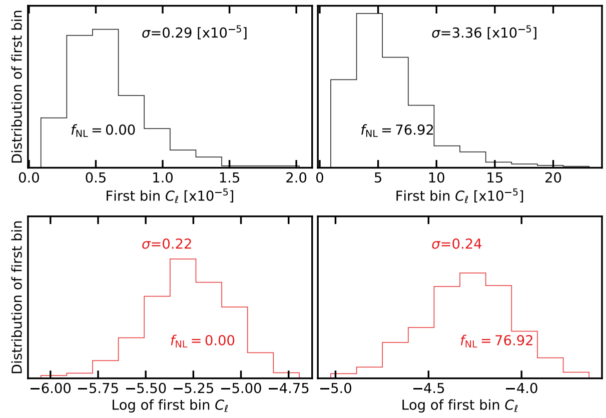

Figure 5. Distribution of the first bin power spectrum for $f_{\rm NL}$ = 0 and 100 mocks.

0. Finally, we multiply the theory correlation function by $\omega^{\rm window}$ and transform the result back to ℓ-space,

$$\hat{\omega}^{\rm model} = \omega^{\rm model}\omega^{\rm window} \tag{9}$$

$$\hat{C}_{\ell}^{\rm model} = 2\pi \int d\theta \hat{\omega}^{\rm model}(\theta) P_{\ell}(\cos\theta). \tag{10}$$

The integral of the galaxy density contrast δ on the footprint is bound to zero, which is often referred to as the *Integral Constraint*. We account for this effect in the modeling by,

$$\hat{C}_{\ell}^{\rm model,IC} = \hat{C}_{\ell}^{\rm model} - \hat{C}_{\ell=0}^{\rm model}\left(\frac{\hat{C}_{\ell}^{\rm window}}{\hat{C}_{\ell=0}^{\rm window}}\right) \tag{11}$$

Fig. 4 shows the mean measured power spectrum of 1000 lognormal density fields (dashed) and best fit theory prediction. light and dark shades represent the 68% error on the mean and one single realization, respectively. DESI footprint mask is applied to the mocks, and even though DESI covers around 40% of the sky, but the window effect is affecting modes down to ℓ = 200. On the other hand, integral constraint only alters the power in the first two bins.

3.2 Measuring Power Spectrum

The quantity that carries cosmological information is galaxy density contrast, δ, which in pixel i is constructed as,

$$\hat{\delta}_i = \frac{\rho_i}{\hat{\bar{\rho}}} - 1, \tag{12}$$

where ρ is the density of galaxies accounted for pixel area $f_{{\rm pix},i}$, which is determined by uniformly distributed random galaxies over footprint, and $\hat{\bar{\rho}}$ is the mean galaxy density directly estimated from the data,

$$\hat{\bar{\rho}} = \frac{\sum_i \rho_i f_{{\rm pix},i}}{\sum_i f_{{\rm pix},i}}. \tag{13}$$

By definition, Eqs. 12 and 13 ensure that the integral of the observed quantity over the footprint vanishes:

$$\sum_i \hat{\delta}_i\, f_{{\rm pix},i} = 0, \tag{14}$$

and this constraint causes an effect commonly referred to as *integral constraint*, which needs to be accounted for in the model. To estimate power spectrum, the galaxy density contrast is expanded in terms of Legendre polynomials,

$$\hat{\delta}_i = \sum_{\ell=0}^{\ell_{\rm max}} \sum_{m=-\ell}^{\ell} a_{\ell m} Y_{\ell m}(\theta_i, \phi_i), \tag{15}$$

where θ, ϕ represent the polar and azimuthal angular coordinates of pixel i center, respectively. The cutoff at $\ell = \ell_{\rm max}$ assumes that modes with $\ell > \ell_{\rm max}$ do not contribute significantly to signal power. The coefficients $a_{\ell m}$ are then obtained by integrating the density contrast field over the total number of non-empty pixels $N_{\rm pix}$ and using the orthogonality of Legendre polynomials:

$$\hat{a}_{\ell m} = \frac{4\pi}{N_{\rm pix}} \sum_{i=1}^{N_{\rm pix}} \hat{\delta}_i\, f_{{\rm pix},i}\, Y^*_{\ell m}(\theta_i, \phi_i), \tag{16}$$

where * represents the complex conjugate. Then, the angular power spectrum estimator is defined as the variance of $\hat{a}_{\ell m}$ coefficients:

$$\hat{C}_{\ell} = \frac{1}{2\ell+1} \sum_{m=-\ell}^{\ell} \hat{a}_{\ell m} \hat{a}^*_{\ell m}. \tag{17}$$

In order to extract $\hat{a}_{\ell m}$ and compute the angular power spectrum, C_{ℓ}, the function ANAFAST is called from HEALPix (Gorski et al. 2005) with the third order iteration of the quadrature to increase the accuracy[4]. Due to the survey geometry implicit in the summation over the non-empty pixels and explicit in $f_{\rm pix,i}$, our estimator does not return an unbiased estimate of power spectrum, as different modes are no longer independent. Therefore, the same effect must be accounted in the modeling of power spectrum.

3.3 Parameter estimation

Signature of local PNG is unique and cannot be reproduced with other cosmological parameters. We allow three parameters to vary;

[4] We refer the reader to `https://healpix.sourceforge.io/pdf/subroutines.pdf`, p. 104-105.

$f_{\rm NL}$, shotnoise, and bias at $z = 0$. Throughout this manuscript, we bin each mode with $\Delta\ell = 2$ between $\ell = 2$ and 20 and $\Delta\ell = 10$ from $\ell = 20$ to 300, while weighting each mode by $2\ell + 1$. We also find that the distribution of power spectrum at the lowest bin, $2 \leq \ell < 12$, is not Gaussian and its standard deviation varies significantly from mocks with $f_{\rm NL} = 0$ to 76.9 (see, Fig. 5). Therefore, we attempt to fit $\log C_\ell$ to make our constraints insensitive to the choice of covariance matrix. The parameter $f_{\rm NL}$ is constrained by maximizing a posterior defined as,

$$-2\ln\mathcal{L} = (\log C(\Theta) - \log\hat{C})^\dagger \mathbb{C}^{-1}(\log C(\Theta) - \log\hat{C}) + \chi^2_{\rm priors}, \quad (18)$$

where Θ represents the parameters, $f_{\rm NL}$, bias at $z = 0$, and shotnoise, all of which are associated with a flat prior, $\chi^2_{\rm priors}$; $C(\Theta)$ is the (binned) theoretical power spectrum including the effects for survey geometry and integral constraint; $\hat{C}$ is the (binned) measured power spectrum; and $\mathbb{C}$ is the covariance matrix constructed from simulations.

3.4 Characterization of residual systematic error

We use the diagnostic tests presented in Rezaie et al 2021 based on cross power spectrum between galaxy density field and imaging maps and mean density contrast as a function of imaging properties to quantify the significance of imaging systematic effects.

3.4.1 Cross Spectrum

Taking $C_\ell^{g,x}$ as the cross power spectrum between galaxy density contrast field and imaging map, one can normalize this quantity by auto power spectrum of imaging map itself:

$$\hat{C}_{x,\ell} = \frac{(\hat{C}_\ell^{g,x})^2}{\hat{C}_\ell^{x,x}}, \quad (19)$$

and then construct a vector from cross spectra against all other imaging maps:

$$\hat{C}_{X,\ell} = [\hat{C}_{x_1,\ell}, \hat{C}_{x_2,\ell}, \hat{C}_{x_3,\ell}, ..., \hat{C}_{x_9,\ell}]. \quad (20)$$

Finally, cross power spectrum χ^2 can be defined as,

$$\chi^2 = C_{X,\ell}^T \mathbb{C}_X^{-1} C_{X,\ell}, \quad (21)$$

where covariance matrix $\mathbb{C}_X =< C_{X,\ell} C_{X,\ell'} >$ is constructed from mocks without systematic effects. This statistics is measured for every mock realization with the leave-one-out technique to construct a histogram, which is then compared to the χ^2 value observed from the DR9. Fig. 6 (top) shows the measured C_X the DR9 sample before and after applying various imaging weights, relative to that of the mocks with $f_{\rm NL} = 0$. The dispersions of mocks with and without PNG are shown with the shade regions for comparison. We bin the C_X measurements from $\ell = 2$ to 20 with $\Delta\ell = 2$. The mean and standard deviation of $\hat{C}_{X,\ell}$ for 1000 mocks with and without $f_{\rm NL}$ are shown in Fig. 6. Extinction and stellar density have the highest cross power spectrum, and then depth in the z band. After applying the first version of weights with linear conservative I which includes extinction and depth-z, the cross power increases against psftsize in the r band. This indicates that only two maps are not sufficient to null out all of the cross correlations. With linear model there is residual power against extinction, depth-z, and psfsize-z; therefore, we apply weights based on a nonlinear model to account for more complex systematic effects.

Fig. 7 (top) shows the histogram of cross spectrum χ^2 from mocks with and without $f_{\rm NL}$. Comparing with the data, the residual is 20014.8 before correction, and after applying the first set of weights, it reduces to 375.1 with p-value XXX. Adding psfsize-z, the linear model reduces the error dow to 195.9 (p-value = XXX). Although using all maps gives the lowest error i.e., 129.2, but it could potentially lead to over-fitting true clustering given how correlated the imaging maps are (see, Fig. 3). On the other hand, the nonlinear method with three maps yields a χ^2 value of 79.3 and p-value of XXX, and adding the stellar density map reduces the error to 70.9 (p-value=XXX). This test clearly shows that a nonlinear approach is desired to get a null test. We further test the stability of our results by extending the highest mode from $\ell = 20$ to 100, or fluctuations over scales as small as 1.8 degrees (see, Fig. 8). The solid line shows how the median of 1000 mocks changes as the highest ℓ increases from 20 to 100. The red circles show the chi2 for the linear approach with three maps and the blue crosses show the chi2 for the nonlinear approach with three maps.

3.4.2 Mean Density

As an alternative test, we calculate the histogram of the density contrast field relative to each imaging map.

$$\delta_x = (\hat{\bar{\rho}})^{-1} \frac{\sum_i \rho_i f_{{\rm pix},i}}{\sum_i f_{{\rm pix},i}}, \quad (22)$$

where the summations are over pixels in each bin of imaging map x. Similarly, we construct the mean density contract vector against all imaging maps,

$$\delta_X = [\delta_{x_1}, \delta_{x_2}, \delta_{x_3}, ..., \delta_{x_9}], \quad (23)$$

and the total residual error as,

$$\chi^2 = \delta_X^T \mathbb{C}_\delta{}^{-1} \delta_X, \quad (24)$$

where the covariance matrix $\mathbb{C}_\delta =< \delta_X \delta_X >$ is constructed from mocks without systematic effects. Fig. 6 (bottom) shows the mean density contrast for the DR9 LRG sample. The shades represent the 1σ level fluctuations observed in 1000 clean mocks with $f_{\rm NL} = 0$ and 100. Before treatment (solid) shows strong correlation around 10% against depth in the z band which is consistent with the cross power spectrum. Beside that, there are strong positive trends against extinction and stellar density at about 5 – 6%. The linear model is able to mitigate most of the systematic effects with only the extinction and depth-z maps as input, however a new trend appears against psfsize-r which is indicative of psfsize dependence in the sample. This finding is in agreement with the cross power spectrum. Even after applying the linear weights there is some residual against depth-z at around 2%, which indicates the systematic effects might be more complex than what can be removed using a linear model. Nonlinear model with three maps (or four maps including the stellar density) is capable of reducing the fluctuations below 2%.

Fig. 7 (bottom) shows the mean density χ^2 observed in the mocks vs DR9 sample before and after applying imaging weights. Linear weights with two maps reduce the chi-2 value from 679.8 (before) to 178.8. The p-value is indicative of remaining systematic effects. Adding psfsize-r does not help much with the p-value even though it reduces the chi-2 to 130. Using all maps with the linear model gives a more reasonable value however it leaves the analysis susceptible to over-fitting true clustering signal. With nonlinear approach two maps as input, the chi-2 is reasonable 74.3 with p-value XXX, and adding the stellar map does not change the p-value much, indicating the trend against stellar density can be explained with the extinction to a great extend.

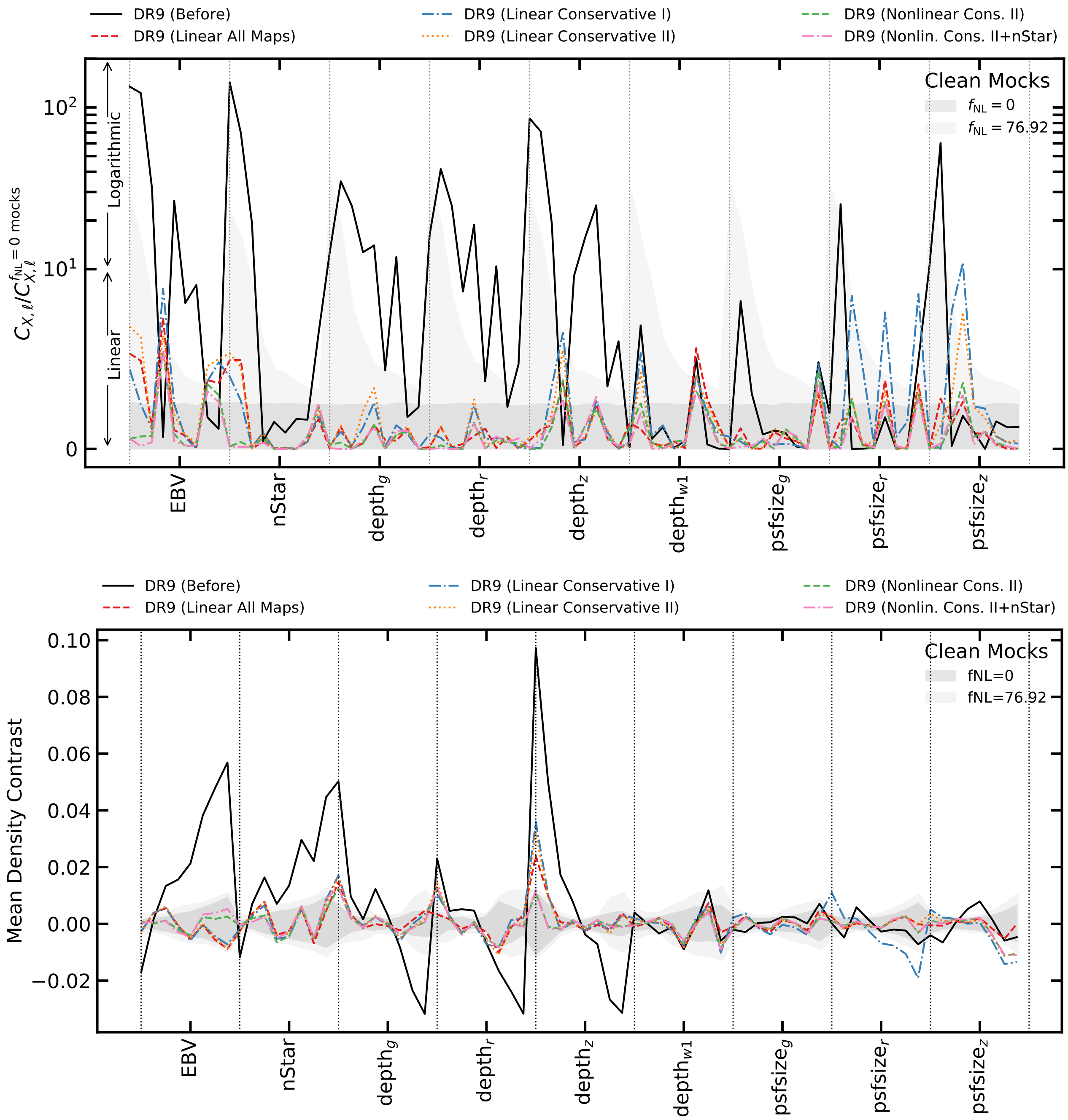

Figure 6. Residual systematic fluctuations of DR9 LRGs against imaging maps. Left: cross spectrum. Right: mean density contrast. Shades represent 1σ dispersion of 1000 clean mocks with and without $f_{\rm NL}$. Solid curve shows the data before applying any weights, while the red dashed shows the data with linear all maps, and blue dot-dashed shows the data with linear cons I, and orange dotted curve shows linear cons II. The nonlinear models are shown with blue dashed and red dot-dashed.

4 RESULTS

This sections presents the constraint on $f_{\rm NL}$ from the DR9 LRG sample. The robustness of constraints are tested against various assumptions and details in survey mask, imaging weights, and calibration of data. The default analysis uses the covariance from $f_{\rm NL}=0$ mocks. We also validate the modeling pipeline and characterize the amount of mitigation bias introduced in $f_{\rm NL}$ after cleaning for systematics.

4.1 DR9 LRGs

Fig. 9 shows the measured power spectrum of DR9 LRGs with different imaging weights, the best fit theory curves, and the mean and 1σ error from the $f_{\rm NL}=0$ lognormal mocks. Power spectra are similar with differences less than ??% for small scales ($\ell > 2$), and as we go to larger scales, the differences become more significant. There is a little difference between linear cons II and linear all maps. This proves that our feature selection procedure has worked to identify the important maps. Comparing linear cons I to linear

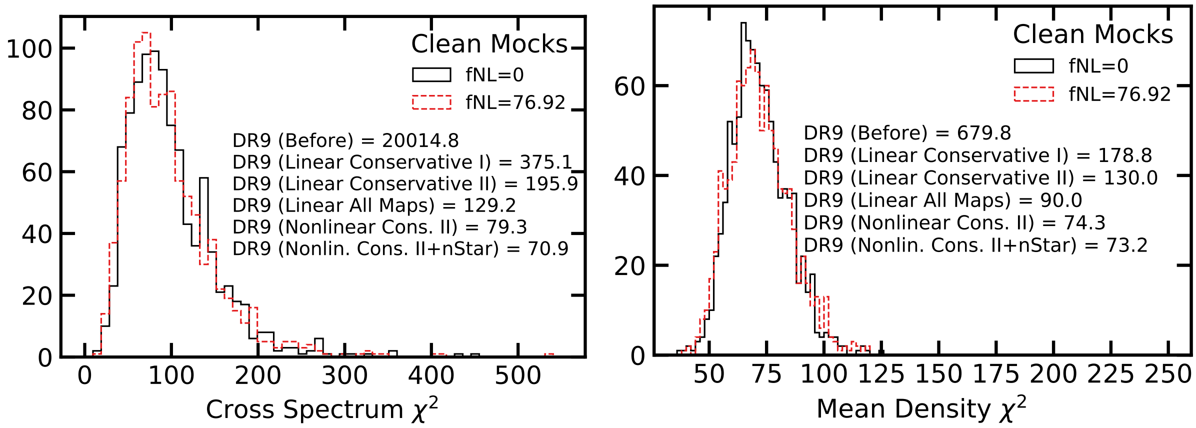

Figure 7. Left: Cross power spectrum χ^2 diagnostic. Right: Mean density contrast diagnostic. The values observed in DR9 before and after linear and nonlinear treatments are quoted and the histograms are constructed from 1000 realizations of clean mocks with $f_{\rm NL}$ = 0 and 76.92.

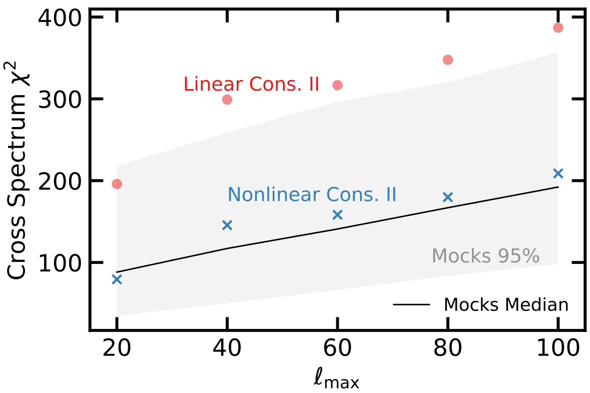

Figure 8. Cross Spectrum χ^2 as a function of the highest mode $\ell_{\rm max}$. The lowest mode is $\ell_{\rm min}$ = 2.

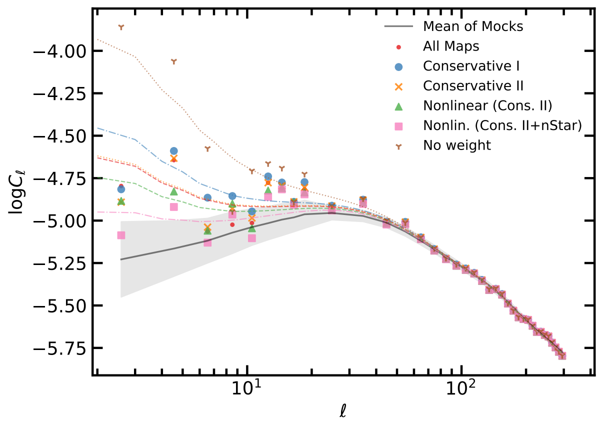

Figure 9. Measured power spectrum of the DR9 LRG sample before and after correcting for systematics with their corresponding best fit theory predictions. The shade represents 1σ error constructed from the $f_{\rm NL}$ = 0 mocks.

cons II, modes with $6 \leq \ell < 10$ are different, indicating scales where psfsize-r is affecting the signal. Comparing nonlinear cons II to linear cons II, modes at the second bin ($4 \leq \ell < 6$) are very different, indicating the nonlinear approach is more flexible to reduce fluctuations on small scales as well large scales.

$f_{\rm NL}$ constraints from DR9 LRG sample is summarized in Table 2. First, we focus on the DESI footprint and then compare constraints obtained from each sub-survey. Fig 10 shows the 2D constraints with 68% and 95% confidence on $f_{\rm NL}$ and b for the DESI footprint from the DR9 sample before (no weight) and after applying different cleaning schemes. No weight constraint at 68% is $98.14 < f_{\rm NL} < 132.89$ with a best fit of 113.18 and marginalized mean of 115.49, and is more than 2σ off from zero. Applying imaging weights shifts constraints to lower $f_{\rm NL}$ values, and b is slightly pulled upward since excess clustering due to systematics is removed. Using all maps with the linear model does not change the results, showing that three maps are sufficient at the linear level to mitigate systematics. As an alternative, using a nonlinear model with three maps shows around 1σ shift, with 68% confidence at $18.91 < f_{\rm NL} < 40.59$, inconsistent with zero for more than 2σ. Adding a template for the local stellar density shift constraints by 1σ, making it consistent with zero. As the most rigorous approach, using all maps and stellar density included results in more than 2σ shift. We emphasize that these shifts to lower $f_{\rm NL}$ are somewhat ex-

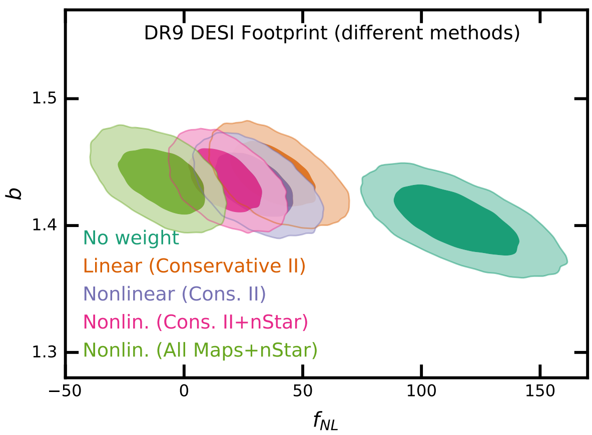

Figure 10. DR9 constraints. DESI footprint before and after applying various cleaning methods.

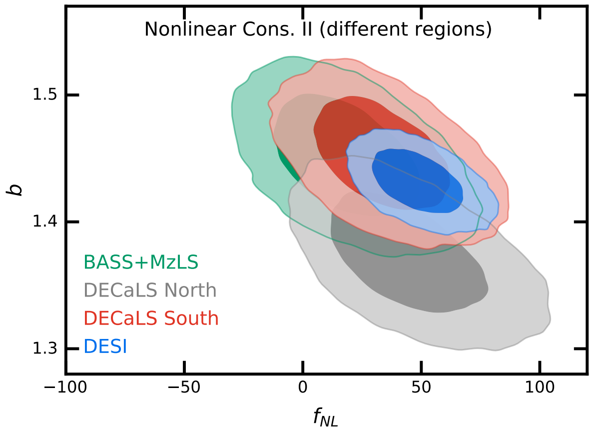

Figure 11. DR9 constraints. Each individual imaging survey versus the whole DESI footprint.

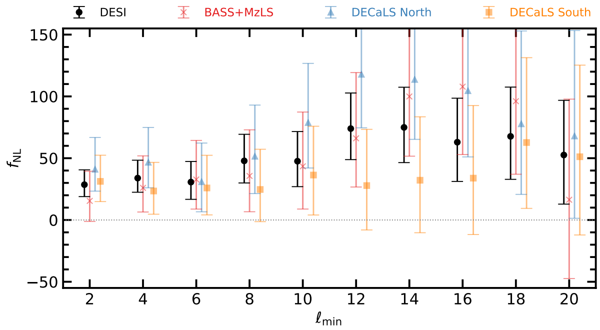

Figure 12. DR9 Constraints. Mean estimates of $f_{\rm NL}$ and its 65% and 95% errorbars after changing the lowest ℓ mode used in fitting.

pected as more input maps results in regressing more modes from cosmological clustering signal. Therefore, we use lognormal mocks to calibrate the amount of signal that is removed in each case and attempt to undo the effect.

We also evaluate the robustness of constraints against various cuts and configurations. First, we compare how constraints from whole DESI footprint compares to those from each survey individually, namely BASS+MzLS, DECaLS Nouth, and DECaLS South. Fig. 11 shows 68% and 95% confidence on $f_{\rm NL}$ and b from each individual survey or all combined as DESI. Constraints from all surveys are consistent and agree with each other within 68%. Both BASS+MzLS and DECaLS South are consistent with zero PNG, but DECaLS North deviates from zero at more than 2σ. Adding the stellar density template does not change constraints from BASS+MzLS much, but it shifts DECaLS North and DECaLS South by 0.5σ and σ, respectively. This might indicate that there are some unresolved issues with stellar contamination in DECaLS North and DECaLS South. We note that differences are more significant when all maps and stellar density are used as input. This is expected as more maps mean the model has more freedom to take out clustering modes. We

Pixel completeness We remove pixels with low completeness from the DESI footprint by applying $f_{\rm pix} > 0.5$, and find that the impact is negligible. Specifically, the cut removes .6% survey area and causes best fit $f_{\rm NL}$ shifts only around 2%, from 28.58 to 28.07, see *comp cut* Table 2. When investigated this impact on each region separately, BASS+MzLS increases around 10%, DECaLS North decreases 1%, and DECaLS South decreases around 5%.

Imaging quality We remove pixels with poor imaging from the DESI footprint by applying the following cuts on imaging properties; $E[B-V] < 0.1$, $nStar < 3000$, $depth_g > 23.2$, $depth_r > 22.6$, $depth_z > 22.5$, $psfsize_g < 2.5$, $psfsize_r < 2.5$, and $psfsize_z < 2$. Overall the constraints are consistent despite best fit and marginalized mean estimates shift. Quantitatively, we lose about 8.2% survey area, and the best fit $f_{\rm NL}$ estimate changes about 2% from 28.58 to 29.16. See *imag cut* in Table 2. For BASS+MzLS only, the imaging cut increases the best fit by 62% from 15.43 to 25.03. For DECaLS North and DECaLS South, the best fit increases by 5% and 15% respectively.

Covariance We now use the mocks with $f_{\rm NL} = 76.92$ to construct a covariance matrix, and with the new covariance we observe a 12% increase in the $f_{\rm NL}$ constraint uncertainties and 11% increase in the best fit estimate of $f_{\rm NL}$.

Lowest ℓ We decrease the largest mode (or increase the lowest ℓ) used in estimating the best fit and 68% confidence intervals. Fig. 12 illustrates the results for the DESI footprint and how they compared to BASS+MzLS, DECaLS North, or DECaLS South only results. Overall we find that the constraints are robust against the largest mode.

External maps We also derive imaging weights using additional external maps for the neutral hydrogen column density (HI) and magnitude calibration errors in the z band (CALIBZ). With the new weights, we find the best fit estimates increase from 41.02 to 55.46 for DECaLS North and from 31.24 to 33.79 for DECaLS South.

Declination cut Our default analysis do not use the spurious islands in DECaLS North and DECaLS South below DEC = -30 to avoid potential calibration issues. PANASTARS are used for calibration below DEC of -30. Without these cuts, best fit $f_{\rm NL}$ estimates increase from 31.24 to 43.79 for DECaLS South and decrease from 41.02 to 41.05. This indicates that indeed there is an issue with DECaLS South below DEC of −30.

Overall we find that the declination cut is necessary for DECaLS South, while adding external templates for HI and CALIBZ, using a different covariance, or applying imaging and completeness cuts do not alter the constraints significantly.

4.2 Lognormal Mocks

Corner plots of the PNG parameter $f_{\rm NL}$ and bias coefficient are shown in Fig. 13 for fitting the mean power spectrum of mocks, with and without $f_{\rm NL}$. Best fit estimates, marginalized mean, 1σ and 2σ confidence intervals are summarized in Tab. 3. Fig 13 (right) shows confidence contours for different combinations of target variable (e.g., either power spectrum or its log transform) and covariance matrix. First we attempt to understand the impact of covariance on confidence intervals. We fit the mean power spectrum of $f_{\rm NL} = 76.9$ mocks or its log transformation using covariance matrices constructed from the same set of mocks or from the $f_{\rm NL} = 0$ mocks. When covariance is consistent with mean, the difference between fitting power spectrum and log of it is only 2%. If a wrong covariance is used for the log power, the effect is only 7%. However, when mean power spectrum of the $f_{\rm NL} = 76.9$ mocks is fit using the covariance matrix estimated from the $f_{\rm NL} = 0$ mocks, the constraints improve by a factor of 5, simply due to a false higher signal to noise ratio. Therefore, we argue that fitting logarithm of power spectrum would remove the need for having $f_{\rm NL}$-dependent covariance matrices and make the constraints less sensitive to covariance construction. Fig. 13 (left) shows the confidence contours for $f_{\rm NL} = 0$ mocks when fit

Table 2. Maximum-A-Posteriori (MAP) and marginalized mean estimates for $f_{\rm NL}$ from fitting power spectrum of DR9 LRGs before and after correcting for systematics. Degree of freedom is 34 (37 data points - 3 parameters).

		$f_{\rm NL}$				
Footprint	Method	Best fit	Mean	68% CL	95% CL	χ^2
DESI	No Weight	113.18	115.49	$98.14 < f_{\rm NL} < 132.89$	$83.51 < f_{\rm NL} < 151.59$	44.4
DESI	Linear (All Maps)	36.05	37.72	$26.13 < f_{\rm NL} < 49.21$	$16.31 < f_{\rm NL} < 62.31$	41.1
DESI	Linear (Conservative I)	49.58	51.30	$38.21 < f_{\rm NL} < 64.33$	$27.41 < f_{\rm NL} < 78.91$	38.8
DESI	Linear (Conservative II)	36.63	38.11	$26.32 < f_{\rm NL} < 49.86$	$16.36 < f_{\rm NL} < 63.12$	39.6
DESI	Nonlinear (Cons. II)	28.58	29.79	$18.91 < f_{\rm NL} < 40.59$	$9.47 < f_{\rm NL} < 52.73$	34.6
DESI	Nonlin. (Cons. II+nStar)	16.63	17.52	$7.51 < f_{\rm NL} < 27.53$	$-1.59 < f_{\rm NL} < 38.49$	35.2
DESI	Nonlin. (All Maps+nStar)	−5.87	−9.19	$-21.45 < f_{\rm NL} < 2.40$	$-33.81 < f_{\rm NL} < 12.06$	39.5
DESI (imag. cut)	Nonlin. (Cons. II)	29.16	30.57	$19.05 < f_{\rm NL} < 42.18$	$9.01 < f_{\rm NL} < 54.81$	35.8
DESI (comp. cut)	Nonlin. (Cons. II)	28.07	29.48	$18.38 < f_{\rm NL} < 40.50$	$8.81 < f_{\rm NL} < 53.10$	34.5
DESI	Nonlin. (Cons. II)+$f_{\rm NL} = 76.92$ Cov	31.62	33.11	$20.94 < f_{\rm NL} < 45.24$	$10.56 < f_{\rm NL} < 59.16$	33.5
BASS+MzLS	Nonlin. (Cons. II)	15.43	19.01	$-1.17 < f_{\rm NL} < 39.43$	$-19.19 < f_{\rm NL} < 63.56$	35.6
BASS+MzLS	Nonlin. (Cons. II+nStar)	13.12	15.39	$-4.59 < f_{\rm NL} < 35.56$	$-24.88 < f_{\rm NL} < 59.31$	34.7
BASS+MzLS	Nonlin. (All Maps+nStar)	−3.73	−6.34	$-27.11 < f_{\rm NL} < 13.75$	$-47.44 < f_{\rm NL} < 33.94$	36.8
BASS+MzLS (imag. cut)	Nonlin. (Cons. II)	25.03	29.12	$6.16 < f_{\rm NL} < 52.44$	$-14.22 < f_{\rm NL} < 80.54$	36.2
BASS+MzLS (comp. cut)	Nonlin. (Cons. II)	16.99	20.90	$0.26 < f_{\rm NL} < 41.76$	$-18.30 < f_{\rm NL} < 67.12$	35.8
DECaLS North	Nonlin. (Cons. II)	41.02	44.89	$23.33 < f_{\rm NL} < 66.78$	$4.96 < f_{\rm NL} < 93.02$	41.1
DECaLS North	Nonlin. (Cons. II+CALIBZ+HI)	55.46	60.44	$36.78 < f_{\rm NL} < 84.05$	$17.86 < f_{\rm NL} < 112.81$	38.4
DECaLS North	Nonlin. (Cons. II+nStar)	31.45	34.78	$14.14 < f_{\rm NL} < 55.79$	$-5.81 < f_{\rm NL} < 80.80$	41.2
DECaLS North	Nonlin. (All Maps+nStar)	0.81	−5.68	$-29.73 < f_{\rm NL} < 16.71$	$-53.15 < f_{\rm NL} < 36.19$	45.1
DECaLS North + islands	Nonlin. (Cons. II)	41.05	44.82	$23.58 < f_{\rm NL} < 66.08$	$6.40 < f_{\rm NL} < 91.42$	40.7
DECaLS North (imag. cut)	Nonlin. (Cons. II)	43.27	48.39	$24.60 < f_{\rm NL} < 72.50$	$4.71 < f_{\rm NL} < 101.42$	35.1
DECaLS North (comp. cut)	Nonlin. (Cons. II)	40.55	44.63	$22.41 < f_{\rm NL} < 67.11$	$3.95 < f_{\rm NL} < 94.06$	41.4
DECaLS South	Nonlin. (Cons. II)	31.24	33.21	$14.89 < f_{\rm NL} < 52.40$	$-5.11 < f_{\rm NL} < 74.35$	30.2
DECaLS South	Nonlin. (Cons. II+CALIBZ+HI)	33.79	37.50	$17.71 < f_{\rm NL} < 57.42$	$-0.31 < f_{\rm NL} < 80.94$	30.8
DECaLS South	Nonlin. (Cons. II+nStar)	14.34	6.28	$-21.19 < f_{\rm NL} < 30.01$	$-53.63 < f_{\rm NL} < 49.51$	31.9
DECaLS South	Nonlin. (All Maps+nStar)	−36.76	−32.01	$-49.38 < f_{\rm NL} < -13.61$	$-65.26 < f_{\rm NL} < 7.52$	31.5
DECaLS South + DEC < −30	Nonlin. (Cons. II)	43.79	46.79	$30.16 < f_{\rm NL} < 63.41$	$16.38 < f_{\rm NL} < 82.72$	23.8
DECaLS South (imag. cut)	Nonlin. (Cons. II)	26.47	23.36	$3.18 < f_{\rm NL} < 47.84$	$-57.69 < f_{\rm NL} < 71.39$	30.0
DECaLS South (comp. cut)	Nonlin. (Cons. II)	29.62	31.76	$13.00 < f_{\rm NL} < 51.58$	$-9.78 < f_{\rm NL} < 74.28$	29.7

is done to the log of mean spectra of $f_{\rm NL} = 0$ mocks for the different regions. We find that the underlying true $f_{\rm NL}$ value is recovered within 2σ confidence. Add a paragraph for the constraining power vs fsky.

Fig 14 shows the best fit estimates for b vs $f_{\rm NL}$ for $f_{\rm NL} = 0$ and $= 76.92$ mocks in the left and right, respectively. Truth values are represented via the dotted lines. The points are color-coded with the minimum χ^2 from fit for each realization. The histograms of best fit $f_{\rm NL}$ estimates are plotted in the background. We obtain $f_{\rm NL} = MU \pm STD$ and $= MU \pm STD$ for the left and right panels, respectively.

With template based mitigation, the measured power spectrum is biased and the amount of bias depends on the number of input templates. We use a linear model with the set of conservative II maps to simulate imaging systematics in our lognormal density fields. Then, we apply the cleaning method based on nonlinear model with Conservative II, Conservative II + nStar, or All Maps + nStar sets of imaging maps to both set of mocks; with or without systematic effects (dashed or soild), and with and without $f_{\rm NL}$. The marginalized mean, confidence intervals, and best fit estimates are presented in Tab 4. Fig 15 shows the true $f_{\rm NL}$ value and the measured $f_{\rm NL}$ value from fitting the mean of mocks. The results for the contaminated mocks before cleaning (No weight) is not shown for clarity. From this graph, then a pair of linear coefficients are to be found for mapping measured $f_{\rm NL}$ to true $f_{\rm NL}$ values. At the first iteration, we think these coefficients should be applied to the values presented in Tab 2.

5 CONCLUSION

ACKNOWLEDGEMENTS

DATA AVAILABILITY

REFERENCES

Akrami Y., et al., 2019, arXiv preprint arXiv:1905.05697

Coles P., Jones B., 1991, Monthly Notices of the Royal Astronomical Society, 248, 1

Dalal N., Dore O., Huterer D., Shirokov A., 2008, Physical Review D, 77, 123514

Dey A., et al., 2018, arXiv preprint arXiv:1804.08657

Gaia Collaboration et al., 2018, A&A, 616, A1

Gorski K. M., Hivon E., Banday A. J., Wandelt B. D., Hansen F. K., Reinecke M., Bartelmann M., 2005, The Astrophysical Journal, 622, 759

Ho S., et al., 2015, J. Cosmology Astropart. Phys., 2015, 040

Komatsu E., Spergel D. N., 2001, Physical Review D, 63, 063002

Myers A. D., et al., 2022, arXiv e-prints, p. arXiv:2208.08518

Pullen A. R., Hirata C. M., 2013, Publications of the Astronomical Society of the Pacific, 125, 705

Schlegel D. J., Finkbeiner D. P., Davis M., 1998, The Astrophysical Journal, 500, 525

Schmittfull M., Seljak U., 2018, Phys. Rev. D, 97, 123540

Slosar A., Hirata C., Seljak U., Ho S., Padmanabhan N., 2008, Journal of Cosmology and Astroparticle Physics, 2008, 031

Weinberg D. H., Mortonson M. J., Eisenstein D. J., Hirata C., Riess A. G., Rozo E., 2013, Physics reports, 530, 87

Xavier H. S., Abdalla F. B., Joachimi B., 2016, Monthly Notices of the Royal Astronomical Society, 459, 3693

Zhou R., et al., 2021, Monthly Notices of the Royal Astronomical Society, 501, 3309

Table 3. Maximum-A-Posteriori (MAP) and marginalized mean estimates for $f_{\rm NL}$ from fitting the mean power spectrum of the mocks. Degree of freedom is 34 (37 data points - 3 parameters).

			$f_{\rm NL}$				
True $f_{\rm NL}$	Footprint	Observable	Best fit	Mean	68% CL	95% CL	χ^2
76.92	DESI	$\log C_\ell$	77.67	77.67	$77.17 < f_{\rm NL} < 78.16$	$76.71 < f_{\rm NL} < 78.64$	38.8
76.92	DESI	C_ℓ	77.67	77.65	$77.17 < f_{\rm NL} < 78.14$	$76.70 < f_{\rm NL} < 78.60$	39.0
76.92	DESI	$\log C_\ell$ + $f_{\rm NL}=0$ cov	77.70	77.71	$77.25 < f_{\rm NL} < 78.17$	$76.81 < f_{\rm NL} < 78.63$	39.9
76.92	DESI	C_ℓ + $f_{\rm NL}=0$ cov	77.03	77.02	$76.93 < f_{\rm NL} < 77.12$	$76.83 < f_{\rm NL} < 77.22$	207.6
0	DESI	$\log C_\ell$	0.36	0.36	$0.06 < f_{\rm NL} < 0.65$	$-0.23 < f_{\rm NL} < 0.94$	35.7
0	DECaLS North	$\log C_\ell$	0.07	0.06	$-0.47 < f_{\rm NL} < 0.60$	$-1.00 < f_{\rm NL} < 1.12$	26.7
0	DECaLS South	$\log C_\ell$	0.67	0.67	$0.13 < f_{\rm NL} < 1.22$	$-0.40 < f_{\rm NL} < 1.75$	34.3
0	BASS+MzLS	$\log C_\ell$	0.83	0.82	$0.25 < f_{\rm NL} < 1.40$	$-0.31 < f_{\rm NL} < 1.96$	39.4

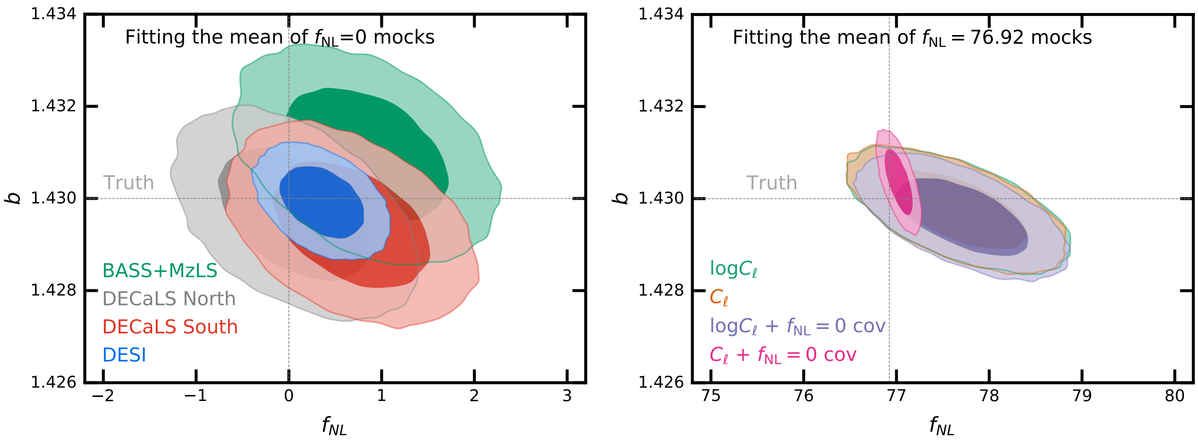

Figure 13. Top: 68% and 95% confidence contours for $f_{\rm NL}=0$ (left) and 100 (right) mocks. Using the $\log C_\ell$ fitting yield constraints that are insensitive to the covariance used. Bottom: best fit estimates from fitting 1000 lognormal mocks with $f_{\rm NL}=0$ (left) and 76.92 (right) in the DESI footprint. The truth values are represented by vertical and horizontal lines.

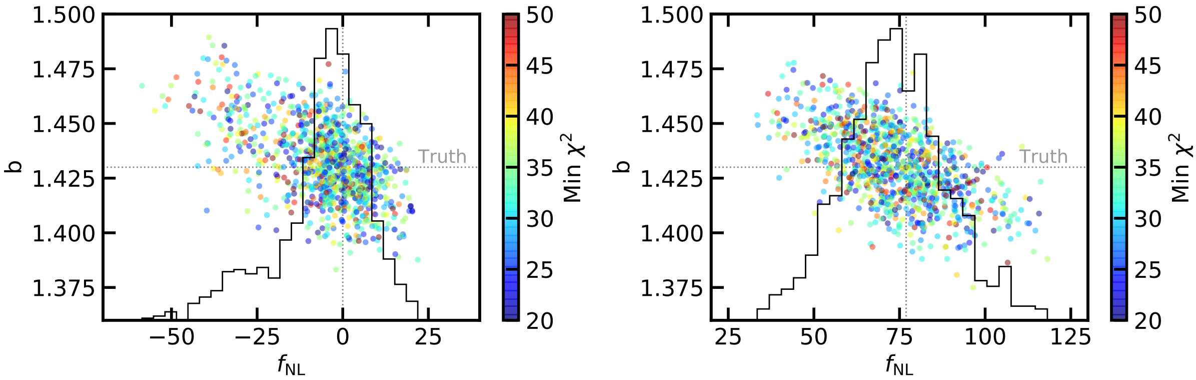

Figure 14. Top: 68% and 95% confidence contours for $f_{\rm NL}=0$ (left) and 100 (right) mocks. Using the $\log C_\ell$ fitting yield constraints that are insensitive to the covariance used. Bottom: best fit estimates from fitting 1000 lognormal mocks with $f_{\rm NL}=0$ (left) and 76.92 (right) in the DESI footprint. The truth values are represented by vertical and horizontal lines.

Zhou R., et al., 2022, arXiv preprint arXiv:2208.08515

Table 4. Best fit and marginalized estimates for $f_{\rm NL}$ from fitting the mean power spectrum of the mocks before and after applying imaging weights.

		$f_{\rm NL}$				
Mock	Method	Best fit	Mean	68% CL	95% CL	χ^2
0	No Weight	0.36	0.36	$0.06 < f_{\rm NL} < 0.65$	$-0.23 < f_{\rm NL} < 0.94$	35.7
0	ConsII	−11.64	−11.65	$-12.00 < f_{\rm NL} < -11.30$	$-12.34 < f_{\rm NL} < -10.97$	86.8
0	ConsII+nStar	−20.14	−20.13	$-20.44 < f_{\rm NL} < -19.82$	$-20.74 < f_{\rm NL} < -19.52$	472.8
0	All Maps+nStar	−26.91	−26.92	$-27.16 < f_{\rm NL} < -26.68$	$-27.39 < f_{\rm NL} < -26.46$	5481.0
Contaminated 0	ConsII	−12.12	−12.13	$-12.48 < f_{\rm NL} < -11.78$	$-12.83 < f_{\rm NL} < -11.44$	94.0
Contaminated 0	ConsII+nStar	−20.97	−20.98	$-21.28 < f_{\rm NL} < -20.67$	$-21.58 < f_{\rm NL} < -20.37$	556.3
Contaminated 0	All Maps+nStar	−28.13	−28.13	$-28.36 < f_{\rm NL} < -27.90$	$-28.59 < f_{\rm NL} < -27.67$	6760.5
76.92	No Weight	77.67	77.67	$77.17 < f_{\rm NL} < 78.16$	$76.71 < f_{\rm NL} < 78.64$	38.8
76.92	ConsII	54.57	54.57	$54.14 < f_{\rm NL} < 55.01$	$53.72 < f_{\rm NL} < 55.45$	603.5
76.92	ConsII+nStar	38.38	38.38	$37.99 < f_{\rm NL} < 38.78$	$37.60 < f_{\rm NL} < 39.16$	537.0
76.92	All Maps+nStar	6.04	6.04	$5.72 < f_{\rm NL} < 6.36$	$5.41 < f_{\rm NL} < 6.67$	694.0
Contaminated 76.92	ConsII	54.01	54.00	$53.57 < f_{\rm NL} < 54.44$	$53.15 < f_{\rm NL} < 54.86$	588.0
Contaminated 76.92	ConsII+nStar	37.48	37.49	$37.09 < f_{\rm NL} < 37.88$	$36.70 < f_{\rm NL} < 38.27$	510.7
Contaminated 76.92	All Maps+nStar	4.59	4.58	$4.26 < f_{\rm NL} < 4.90$	$3.95 < f_{\rm NL} < 5.22$	649.7

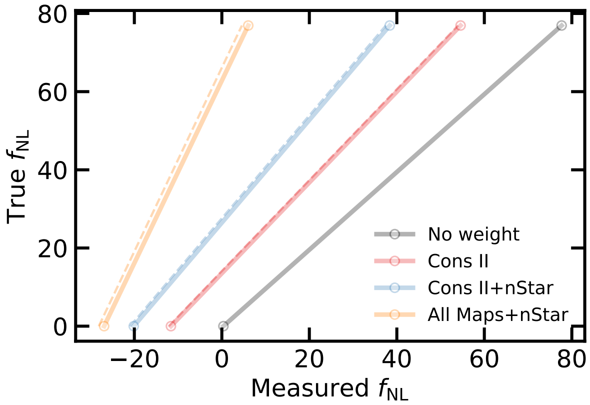

Figure 15. True $f_{\rm NL}$ vs measured $f_{\rm NL}$ from mocks with (dashed) and without systematics (solid).

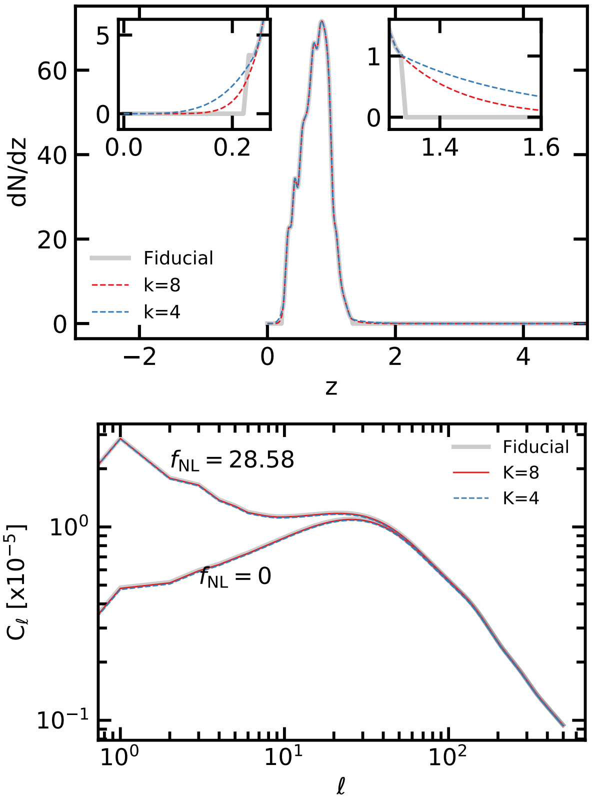

Figure A1. Top: Redshift distribution of LRGs. Bottom: Power spectrum given various dN/dz treatments for two arbitrary $f_{\rm NL}$ values.

APPENDIX A: REDSHIFT DISTRIBUTION

Redshift distribution of LRGs is constructed from the DESI SV data release of Denali with the same selection. The fiducial distribution only covers the redshift range from 0.2 to 1.35. Below we test the impact of LRG dN/dz on the angular power spectrum.

This paper has been typeset from a TEX/LATEX file prepared by the author.